IET Renewable Power Generation

Research Article

IET Journals
The Institution of Engineering and Technology

Modified demagnetisation control strategy for low-voltage ride-through enhancement in DFIG-based wind systems

ISSN 1752-1416
Received on 2nd October 2019
Revised 3rd December 2020
Accepted on 7th December 2020
doi: 10.1049/iet-rpg.2019.1128
www.ietdl.org

Manoj Kumar Senapati[1], Chittaranjan Pradhan[2] ✉, Paresh Kumar Nayak[3], Sanjeevikumar Padmanaban[4], Terje Gjengedal[2]

[1]*Department of Electrical Engineering, Government College of Engineering, Keonjhar, India*
[2]*Department of Electrical Sciences, UiT The Arctic University of Norway, Narvik Campus, Norway*
[3]*Department of Electrical Engineering, Indian Institute of Technology (ISM), Dhanbad, India*
[4]*Department of Energy Technology, Aalborg University Esbjerg, Denmark*
✉ *E-mail: chittaranjan.pradhan@uit.no*

Abstract: The large-scale wind energy conversion systems (WECSs) based on doubly-fed induction generators (DFIGs) are very popular in recent years due to the numerous technical and economic benefits. With the increasing penetration level of wind energy, the latest grid codes require the DFIG-based WECSs to remain connected to the grid under grid fault scenarios and deliver the required reactive power into the grid. However, the direct connection of the stator of the DFIG to the grid makes it prone to grid disturbances, especially to voltage sag. This study proposes a modified demagnetisation control strategy to enhance the low-voltage ride-through (LVRT) capability of the DFIG under grid faults. The proposed control strategy is implemented in a coordinated approach by using the existing demagnetisation control and the addition of an external resistance in the stator side of the DFIG. The demagnetisation control damps the direct current component of the stator flux and the external resistance accelerates the damping of the transient flux by decreasing the time constant and hence, enhancing the LVRT capability of DFIG. The effectiveness of the proposed control strategy is demonstrated under both symmetrical and asymmetrical grid faults simulated system through MATLAB/Simulink®. The comparative results justify the merits of the proposed methodology.

Nomenclature

v_{ro}	induced emf by rotor flux, V
e_{rf}	forced component of emf, V
e_{rn}	natural component of emf, V
i_m	magnetising rotor current, A
i_r	rotor current, A
i_s	stator current, A
L_m	magnetising rotor inductance, H
L_r	rotor inductance, H
L_s	stator inductance, H
p	dip of depth
R_{ext}	external stator resistance, Ω
R_r	rotor resistance, Ω
R_s	stator resistance, Ω
t	instantaneous time, s
t_0	starting time of the fault, s
t_1	clearance time of the fault, s
V_{dc}	DC-link voltage, V
V_r	rotor voltage, V
V_{rf}	forced rotor voltage, V
V_{rn}	natural rotor voltage, V
V_{ro}	open-circuit rotor voltage, V
V_s	stator voltage, V
φ_r	rotor flux, Wb
φ_s	stator flux, Wb
φ_{sf}	forced stator flux, Wb
σ	rotor leakage coefficient
τ_s	time constant, s
ω_r	angular speed of rotor flux, r.p.m.
ω_s	angular speed of stator flux, r.p.m.
$*r$	*superscript denoted for the rotor reference frame
*1,2,0	*subscript denoted for positive-, negative-, and zero-sequence components, respectively

1 Introduction

In recent times, wind energy has been proven a popular alternative renewable source for electricity production globally due to the various technical, economic, and environmental benefits [1]. In 2011, 3.5% of the global electricity demand was produced from wind and this figure is expected to rise approximately to 16% by 2030 [2]. The present-day large-scale wind farms, mostly use doubly-fed induction generator (DFIG) for bulk power generation because of its variable speed constant frequency ability, excellent power control capability, and requirement of lower rating converters result in reduced converter cost and power losses [3–5]. However, as the stator terminals of the DFIG are directly connected to the grid, it is more sensitive to grid disturbances, especially to voltage sags. The dips in grid voltage cause a large transient over-current in the rotor circuit of the DFIG [6]. As a result, the protection circuits will be activated and DFIG is disconnected from the grid to protect the rotor-side converter (RSC). However, due to the increasing penetration of wind power, the revised grid codes require the wind farms to remain connected to the grid under grid-voltage sags and should actively contribute to maintaining the power system stability by supplying reactive power to the grid [7]. This is termed as low-voltage ride-through (LVRT) capability. Different control strategies are reported in the literature with an intention to improve the LVRT capability of the DFIG-based wind farm during grid-voltage sag scenarios.

The installation of a crowbar circuit across the rotor terminals of the DFIG is the most commonly used LVRT solution. It protects the rotor converters during voltage sags by diverting current from the RSC and rapidly de-energising the rotor [8]. However, a crowbar circuit converts the DFIG to a simple induction machine, which draws significant reactive power from the grid under voltage sags and hence, deteriorates the voltage sag further. Reactive power

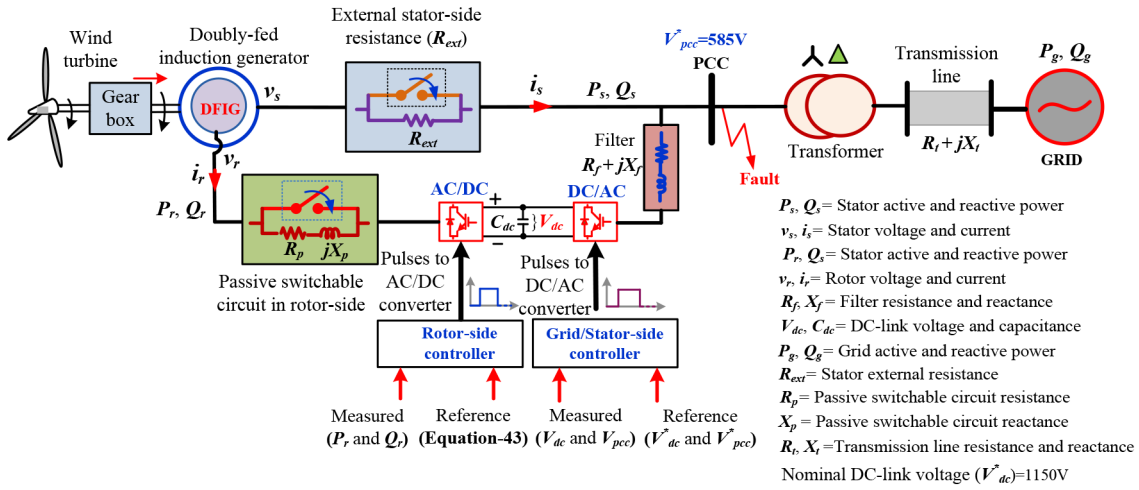

Fig. 1 *Schematic diagram of the grid-connected DFIG-based wind system for LVRT control*

support during grid-voltage sags is provided through the installation of flexible alternating current transmission system devices such as a static VAR compensator or static synchronous compensator [9, 10]. Alternative solutions based on extra power electronics equipment such as series-connected grid-side converter (GSC) [11] and dynamic voltage restorers [12] are employed to keep stator voltage constant during grid-voltage sags. However, the installation of additional converters not only increases the cost but also increases control complexity.

In practice, the methodologies based on the modification of DFIG converter topologies and control strategies are more attractive in achieving the required LVRT capability due to their easy implementation and low cost. A comprehensive overview of LVRT-control methodologies of the wind generators is discussed in [13, 14]. In [11], a feed-forward transient current control approach is proposed in which an additional feed-forward transient compensation (FFTC) is introduced to a conventional current regulator to limit the rotor transient currents and minimise the occurrence of crowbar interruptions during grid faults. An FFTC control scheme with a proportional–integral–resonant current regulator is proposed to enhance the LVRT capability of DFIG during both balanced and unbalanced grid faults [12]. In [15], controllers are designed for both RSC and GSC of the DFIG using a linear quadratic output-feedback decentralised control strategy to enhance voltage stability margins. The designed controllers limit the current oscillations, the peak value of the rotor current, and the direct current (DC)-link voltage fluctuations. In [16], a virtual damping flux-based methodology is proposed to suppress the rotor over-current by smoothing the torque and reactive power thereby improves the LVRT performance of the DFIG. In [17], a control strategy is proposed to improve the LVRT performance of DFIG by using a virtual resistance that limits the rotor-side over-current during grid-voltage sags. Influence of demagnetization control to LVRT ability of DFIG is analysed [18]. A demagnetisation control strategy immune to system parameter variation is proposed to enhance the LVRT functionality of DFIG under the balanced grid fault [19]. In [20], a scaled current tracking control strategy is proposed for RSC to enhance its LVRT capacity, and also, the scheme helps in reducing the electromagnetic torque oscillations without flux observation. The feasibility of the control strategy is validated through both simulation and experimental results. The dynamic voltage and current assignment strategies are proposed for the DFIG-based wind power system using a nine-switch converter [21]. It is demonstrated that the LVRT performance of the DFIG can be improved by suppressing the rotor-side over-current under symmetrical grid-voltage dips. The above-mentioned control strategies are tested mostly for balanced voltage sags to improve the LVRT capability of DFIG.

In [22–26], control schemes based on active and passive LVRT compensators are reported to improve the LVRT ability DFIG under both balanced and unbalanced grid-voltage sags. These approaches reduce the oscillations of rotor over-current, torque oscillations, and the DC-link over-voltage. Moreover, it compensates for the grid-voltage fluctuations by supplying reactive power to the grid. Synchronous flux weakening control with flux linkage prediction is proposed to enhance the LVRT ability of the DFIG by reducing the over-current transients under both symmetric and asymmetric grid-voltage dips [25]. A modified DC-chopper is proposed to improve the LVRT capacity of DFIG under both symmetrical and asymmetrical grid faults [26]. This topology is capable of limiting the high rotor transient overcurrent and the stator current in addition to controlling the DC-link voltage during the fault condition. However, these LVRT solutions are less preferable because of their high cost and control complexity. The aforementioned study clearly indicates that solutions based on novel control methods are attractive to improve the LVRT performance of DFIG. Since demagnetisation control is proposed to counteract the natural component of the stator flux and is further modified to get rid of system parameter dependency. This paper proposes an improved demagnetisation control (IDC) approach for the DFIG, immune to system parameter variations, and uncertainties.

The main contributions of the present paper are summarised as below:

- Development of a modified demagnetisation control strategy with a passive switchable type circuit (i.e. series resistance and inductance as shown in Fig. 1) in the rotor-side for DFIG-based wind energy conversion system (WECS) for improving the LVRT performance.
- An external resistance is included in the stator-side terminal of the DFIG, which accelerates the net resistance and hence, decreases the time constant resulting in transitory flux damps at a faster rate and enhances the LVRT capability.
- The performance of the proposed control strategy is compared with some existing approaches to establish its superiority under both symmetrical and asymmetrical grid faults.

The rest of the paper is organised as follows. The principal modelling and analysis of DFIG under symmetrical/unsymmetrical fault scenarios are exemplified in Section 2. In Section 3, the detailed configuration and operation of the proposed demagnetisation control strategy are provided. The simulation results are presented in Section 4. Finally, the conclusion of the proposed work is provided in Section 5.

2 Modelling and analysis of DFIG under symmetrical/unsymmetrical scenarios

The basic configuration and connection diagram of the DFIG-based grid-connected power system is shown in Fig. 1 [19]. The presented WECS comprises a wind turbine (WT), gearbox, asynchronous DFIG, grid/stator-side converter, RSC, and its control mechanism. The stator of the DFIG is directly connected to

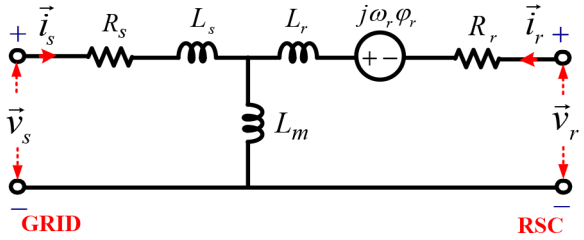

Fig. 2 *Equivalent circuit diagram of DFIG with the stationary stator reference frame*

the grid through a transformer and the rotor is connected to the grid by a back-to-back converter. The RSC enables the variable speed operation of the WT to extract the desired wind power and the GSC regulates the DC-bus voltage for secure and stable operation. In this section, the modelling of DFIG and a comprehensive analytical study of the proposed modified demagnetisation control strategy is presented to enhance the LVRT capability of the DFIG during grid faults.

2.1 Mathematical modelling of DFIG

It is well known that Park's model is commonly used for modelling the induction machine (e.g. DFIG) [27, 28]. For simplifying the analysis, all the rotor variables are referred to as the stator side. Even though a synchronous rotating reference frame is often employed for modelling the DFIG, a stationary stator-oriented reference frame is more suitable for analysing the grid fault (i.e. especially to voltage sag) [19, 28, 29]. Hence, in this study, a stationary reference frame is considered for modelling of the DFIG. For simplicity, linear magnetic circuits are assumed in DFIG modelling. The Park's equivalent model of the DFIG in the stationary stator reference frame is illustrated in Fig. 2. Using the motor convention of the DFIG, the generalised stator and rotor voltage equations for the stationary stator reference frame are expressed as follows [28, 29]:

$$\boldsymbol{v}_{\mathrm{s}} = R_{\mathrm{s}}\boldsymbol{i}_{s} + \frac{\mathrm{d}\boldsymbol{\varphi}_{\mathrm{s}}}{\mathrm{d}t} \tag{1}$$

$$\boldsymbol{v}_{\mathrm{r}} = R_{\mathrm{r}}\boldsymbol{i}_{\mathrm{r}} + L_{\mathrm{r}}\frac{\mathrm{d}\boldsymbol{\varphi}_{\mathrm{r}}}{\mathrm{d}t} - \mathrm{j}\omega_{\mathrm{r}}\boldsymbol{\varphi}_{\mathrm{r}} \tag{2}$$

$$\boldsymbol{\varphi}_{\mathrm{s}} = L_{\mathrm{s}}\boldsymbol{i}_{\mathrm{s}} + L_{\mathrm{m}}\boldsymbol{i}_{\mathrm{r}} \tag{3}$$

$$\boldsymbol{\varphi}_{\mathrm{r}} = L_{\mathrm{r}}\boldsymbol{i}_{\mathrm{r}} + L_{\mathrm{m}}\boldsymbol{i}_{\mathrm{s}} \tag{4}$$

$$\Rightarrow\ \boldsymbol{\varphi}_{\mathrm{r}} = \frac{L_{\mathrm{m}}}{L_{\mathrm{s}}}\boldsymbol{\varphi}_{\mathrm{s}} + \sigma L_{\mathrm{r}}\boldsymbol{i}_{\mathrm{r}} \quad \text{with} \quad \sigma = 1 - \frac{L_{\mathrm{m}}^2}{L_{\mathrm{s}}L_{\mathrm{r}}} \tag{5}$$

where the subscripts 's' and 'r' represent stator and rotor parameters, respectively. φ, v, R, L, and $\boldsymbol{i}$ represent the magnetic flux, voltage, resistance, inductance, and current, respectively. L_{m}, ω_{r}, and σ indicate the magnetising inductance, electrical speed of rotor, and leakage coefficient, respectively.

Substituting (5) in (2), the rotor voltage in terms of the rotor reference frame can be expressed as follows:

$$\boldsymbol{v}_{\mathrm{r}}^{\mathrm{r}} = \frac{L_{\mathrm{m}}}{L_{\mathrm{s}}}\left(\frac{\mathrm{d}}{\mathrm{d}t} - \mathrm{j}\omega_{\mathrm{r}}\right)\boldsymbol{\varphi}_{\mathrm{s}} + \left(R_{\mathrm{r}} + \sigma L_{\mathrm{r}}\left(\frac{\mathrm{d}}{\mathrm{d}t} - \mathrm{j}\omega_{\mathrm{r}}\right)\right)\boldsymbol{i}_{\mathrm{r}} \tag{6}$$

The rotor voltage expressed in (6) can be divided into two parts. The first part represents the voltage induced in the rotor circuit by the stator flux which is denoted as $\boldsymbol{v}_{\mathrm{r0}}$. The second part denotes the voltage drop in the rotor circuit impedance due to the rotor current. For open-circuit condition ($\boldsymbol{i}_{\mathrm{r}} = 0$), the rotor voltage (derived from (6)) is expressed as

$$\boldsymbol{v}_{\mathrm{ro}}^{\mathrm{r}} = \frac{L_{\mathrm{m}}}{L_{\mathrm{s}}}\left(\frac{\mathrm{d}}{\mathrm{d}t} - \mathrm{j}\omega_{\mathrm{r}}\right)\boldsymbol{\varphi}_{\mathrm{s}} \tag{7}$$

In (6), the second part will be a non-zero value when the current flows through the rotor circuit. After inserting (7) into (6), (6) is modified as follows [19, 28]:

$$\boldsymbol{v}_{\mathrm{r}}^{\mathrm{r}} = \boldsymbol{v}_{\mathrm{ro}}^{\mathrm{r}} + \left(R_{\mathrm{r}} + \sigma L_{\mathrm{r}}\left(\frac{\mathrm{d}}{\mathrm{d}t} - \mathrm{j}\omega_{\mathrm{r}}\right)\right)\boldsymbol{i}_{\mathrm{r}} \tag{8}$$

2.2 System operation under symmetrical grid fault

During normal operation of the DFIG, the stator voltage space vector ($\boldsymbol{v}_{\mathrm{s}}$) rotates at synchronous speed (ω_{s}) with a constant amplitude of V_{s} and is expressed as

$$\boldsymbol{v}_{\mathrm{s}} = V_{\mathrm{s}}\mathrm{e}^{\mathrm{j}\omega_{s}t} \tag{9}$$

After neglecting the stator resistance (R_{s}) and inserting (9) in (1), the stator flux is derived as follows:

$$\boldsymbol{\varphi}_{\mathrm{s}} = \frac{V_{\mathrm{s}}}{\mathrm{j}\omega_{\mathrm{s}}}\mathrm{e}^{\mathrm{j}\omega_{s}t} \tag{10}$$

Let us assume a symmetrical fault occurs at the time (t) = t_0 in the grid (i.e. point of common coupling (PCC)) that causes a balanced voltage dip of depth (p) and recovers at the time t_1. For the symmetrical fault, the stator voltage in the time domain can be presented as follows [29]:

$$\boldsymbol{v}_{\mathrm{s}} = \begin{cases} V_{\mathrm{s}}\mathrm{e}^{\mathrm{j}\omega_{s}t}, & (t < t_{\mathrm{o}}) \\ (1-p)V_{\mathrm{s}}\mathrm{e}^{\mathrm{j}\omega_{s}t}, & (t_{\mathrm{o}} \le t < t_1) \\ V_{\mathrm{s}}\mathrm{e}^{\mathrm{j}\omega_{s}t}, & (t \ge t_1) \end{cases} \tag{11}$$

Furthermore, considering the rotor in an open-circuit scenario ($\boldsymbol{i}_{\mathrm{r}} = 0$) and solving (1) and (3), the stator flux can be obtained as follows:

$$\frac{\mathrm{d}\boldsymbol{\varphi}_{\mathrm{s}}}{\mathrm{d}t} = \boldsymbol{v}_{\mathrm{s}} - \frac{R_{\mathrm{s}}}{L_{\mathrm{s}}}\boldsymbol{\varphi}_{\mathrm{s}} \tag{12}$$

In the time domain, for $t > t_{\mathrm{o}}$, after computing (12), it has two parts (i.e. homogeneous and non-homogeneous). The homogeneous solution gives the natural response of (12), which is referred to as the natural flux ($\boldsymbol{\varphi}_{\mathrm{sn}}$) and is expressed as follows [19]:

$$\boldsymbol{\varphi}_{\mathrm{sn}} = \frac{pV_{\mathrm{s}}}{\mathrm{j}\omega_{\mathrm{s}}}\mathrm{e}^{-((t-t_0)/\tau_{\mathrm{s}})} = \varphi_{n0}e^{-((t-t_0)/\tau_{\mathrm{s}})} \quad (t_{\mathrm{o}} < t < t_1) \tag{13}$$

where $\tau_{\mathrm{s}} = L_{\mathrm{s}}/R_{\mathrm{s}}$ is the time constant of the stator flux. L_{s}, R_{s}, and ω_{s} are the stator inductance, resistance, and synchronous speed, respectively. φ_{n0} is the initial flux. In practice, the natural flux ($\boldsymbol{\varphi}_{\mathrm{sn}}$) is a transient flux that guarantees that no discontinuities appear in the magnetic state of the machine when the operating point changes.

The non-homogeneous solution corresponds to the forced flux ($\boldsymbol{\varphi}_{\mathrm{sf}}$) and is the flux at a steady state. Neglecting the stator resistance, the steady-state flux (i.e. the flux imposed by the stator voltage) can be presented as follows:

$$\boldsymbol{\varphi}_{\mathrm{sf}} = \begin{cases} \dfrac{V_{\mathrm{s}}}{\mathrm{j}\omega_{\mathrm{s}}}\mathrm{e}^{\mathrm{j}\omega_{s}t}, & (t < t_{\mathrm{o}}) \\ \dfrac{(1-p)V_{\mathrm{s}}}{\mathrm{j}\omega_{\mathrm{s}}}\mathrm{e}^{\mathrm{j}\omega_{s}t}, & (t_{\mathrm{o}} < t < t_1) \end{cases} \tag{14}$$

From (13), it can be derived that the flux is a state variable, which cannot change instantaneously from the first value to the second one. On the contrary, the flux changes progressively. Moreover, it can be observed that $\boldsymbol{\varphi}_{\mathrm{sf}}$ is proportional to the grid voltage, and the dip in φ_{sf} is (1−p) times the pre-fault value during a symmetrical fault.

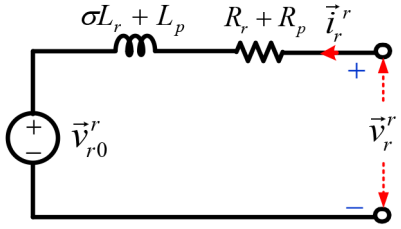

Fig. 3 *Modified equivalent circuit diagram with external rotor resistance and reactance of DFIG viewed from the rotor side*

Furthermore, the initial flux (φ_{r0}) is obtained from the initial condition ($t = t_0$) by considering that the stator flux must be identical immediately before and after the fault as follows [29]:

$$\boldsymbol{\varphi}_{\mathrm{s}}(t_0^-) = \boldsymbol{\varphi}_{\mathrm{s}}(t_0^+) \Rightarrow \boldsymbol{\varphi}_{\mathrm{sf}}(t_0^-) = \boldsymbol{\varphi}_{\mathrm{sf}}(t_0^+) + \boldsymbol{\varphi}_{\mathrm{sn}}(t_0^+) \tag{15}$$

Assuming $t_0 = 0$ and combing (12), (14), and (15), the stator flux during balanced voltage dip can be expressed as follows:

$$\boldsymbol{\varphi}_{\mathrm{s}}(t) = \frac{(1-p)V_{\mathrm{s}}}{\mathrm{j}\omega_{\mathrm{s}}}\mathrm{e}^{\mathrm{j}\omega_{\mathrm{s}}t} + \frac{pV_{\mathrm{s}}}{\mathrm{j}\omega_{\mathrm{s}}}\mathrm{e}^{-(t/\tau_{\mathrm{s}})} \tag{16}$$

Meanwhile, the forced ($\boldsymbol{\varphi}_{\mathrm{sf}}$) and natural ($\boldsymbol{\varphi}_{\mathrm{sn}}$) components of the stator fluxes induce their corresponding open-circuit forced ($\boldsymbol{v}_{\mathrm{rf}}$) and natural ($\boldsymbol{v}_{\mathrm{rn}}$) rotor voltages, respectively. Substituting (13) in (7), $\boldsymbol{v}_{\mathrm{rf}}$ is obtained as (17) and inserting (16) into (7), $\boldsymbol{v}_{\mathrm{rn}}$ is evaluated as (18) [19]

$$\boldsymbol{v}_{\mathrm{rf}} = (1-p)V_{\mathrm{s}}\frac{sL_{\mathrm{m}}}{L_{\mathrm{s}}}\mathrm{e}^{\mathrm{j}\omega_{\mathrm{s}}t} \tag{17}$$

$$\boldsymbol{v}_{\mathrm{rn}} = -\frac{L_{\mathrm{m}}}{L_{\mathrm{s}}}\left(\frac{1}{\tau_{\mathrm{s}}} + \mathrm{j}\omega_{\mathrm{r}}\right)\frac{pV_{\mathrm{s}}}{\mathrm{j}\omega_{\mathrm{s}}}\mathrm{e}^{-(t/\tau_{\mathrm{s}})} \tag{18}$$

where $s = (\omega/\omega_{\mathrm{s}}) = (\omega_{\mathrm{s}} - \omega_{\mathrm{r}}/\omega_{\mathrm{s}})$. s, ω, ω_s and ω_r are slip and slip frequency, synchronous speed, and rotor angular speed, respectively. In DFIG, the value of slip (s) lies between −0.3 and 0.3 [17]. Neglecting the term $1/\tau_{\mathrm{s}}$ in (18), $\boldsymbol{v}_{\mathrm{rn}}$ can be modified as follows:

$$\boldsymbol{v}_{\mathrm{rn}} \simeq -\frac{L_{\mathrm{m}}}{L_{\mathrm{s}}}\frac{\omega_{\mathrm{r}}}{\omega_{\mathrm{s}}}pV_{\mathrm{s}}\mathrm{e}^{-(t/\tau_{\mathrm{s}})} \tag{19}$$

Furthermore, by adding (15) and (16), the rotor voltage for open-circuit condition ($\boldsymbol{i}_{\mathrm{r}} = 0$) in the rotor reference frame can be expressed as follows [19]:

$$\boldsymbol{v}_{\mathrm{r0}}^{\mathrm{r}} \simeq V_{\mathrm{s}}\frac{L_{\mathrm{m}}}{L_{\mathrm{s}}}\left[s(1-p)\mathrm{e}^{\mathrm{j}\omega_{\mathrm{s}}t} - p(1-s)\mathrm{e}^{-(\mathrm{j}\omega_{\mathrm{r}}t + (t/\tau_{\mathrm{s}}))}\right] \tag{20}$$

The magnitude of the induced open-circuit rotor voltage is derived from (20) and expressed as follows:

$$V_{\mathrm{r0}}^{\mathrm{r}} \simeq V_{\mathrm{s}}\frac{L_{\mathrm{m}}}{L_{\mathrm{s}}}(s-p) \tag{21}$$

Now, the actual rotor voltage and current in terms of $\boldsymbol{v}_{\mathrm{r0}}^{\mathrm{r}}$ for the rotor reference frame can be evaluated as follows:

$$\boldsymbol{v}_{\mathrm{r}}^{\mathrm{r}} = \vec{v}_{\mathrm{ro}}^{\,\mathrm{r}} + (R_{\mathrm{r}} + \mathrm{j}s\omega_{\mathrm{s}}\sigma L_{\mathrm{r}})\boldsymbol{i}_{\mathrm{r}}^{\mathrm{r}} \Rightarrow \boldsymbol{i}_{\mathrm{r}}^{\mathrm{r}} = \frac{\boldsymbol{v}_{\mathrm{r}}^{\mathrm{r}} - \boldsymbol{v}_{\mathrm{r0}}^{\mathrm{r}}}{R_{\mathrm{r}} + \mathrm{j}s\omega_{\mathrm{s}}\sigma L_{\mathrm{r}}} \tag{22}$$

In general, during normal operation and for small voltage dip, the induced open-circuit voltage ($\boldsymbol{v}_{\mathrm{r0}}^{\mathrm{r}}$) of the rotor is low and hence the value of the rotor current lies in the safe operating limit/constraint. However, for fault and larger dips, the voltage induced by the stator flux exceeds the maximum limits of the converter, and the rotor current increases transitorily. Hence, a passive switchable circuit is added to the rotor circuit (i.e. series resistance and inductance) as shown in Fig. 1 to regulate/limit the rotor current in the case of severe disturbances. Whenever the actual rotor current ($\boldsymbol{i}_{\mathrm{r}}$) goes beyond its threshold limit ($\boldsymbol{i}_{\mathrm{r-th}}$), the rotor current will be limited by the series resistance (R_{p}) and inductance (L_{p}), for a stable and secure power system operation and protect the circuit from over-current. However, for normal operational scenarios, the power electronics switch will be activated (i.e. the switch is closed) to avoid the continuous voltage drop and power loss due to R_{p} and L_{p} parameters. The comparative signal between $\boldsymbol{i}_{\mathrm{r}}$ and $\boldsymbol{i}_{\mathrm{r-th}}$ are used to generate the switching pulses. The modified equivalent circuit diagram with an external rotor resistance and reactance (i.e. R_{p} and X_{p}) of DFIG for the rotor reference frame is presented in Fig. 3 and the corresponding rotor voltage equation is derived as follows:

$$\boldsymbol{v}_{\mathrm{r}}^{\mathrm{r}} = \boldsymbol{v}_{\mathrm{ro}}^{\mathrm{r}} + (R_{\mathrm{p}} + R_{\mathrm{r}})\boldsymbol{i}_{\mathrm{r}}^{\mathrm{r}} + \mathrm{j}s\omega_{\mathrm{s}}(L_{\mathrm{p}} + \sigma L_{\mathrm{r}})\boldsymbol{i}_{\mathrm{r}}^{\mathrm{r}} \tag{23}$$

2.3 System operation under unbalanced/asymmetrical grid fault

The Fortescue transforms function is a well-known method that is used for analysing the effect of the asymmetrical (i.e. unbalanced) systems on the voltage performances of the DFIG [30]. According to this theory, the three-phase unbalanced voltages can be expressed as a sum of three balanced phasor components known as positive, negative, and zero sequence. Thus, the unbalanced stator voltage phasor ($\boldsymbol{v}_{\mathrm{s}}$) can be expressed as follows [29]:

$$\boldsymbol{v}_{\mathrm{s}} = \boldsymbol{v}_1 + \boldsymbol{v}_2 + \boldsymbol{v}_0 = V_1\mathrm{e}^{\mathrm{j}\omega_{\mathrm{s}}t} + V_2\mathrm{e}^{\mathrm{j}\omega_{\mathrm{s}}t} + V_0 \tag{24}$$

where V_1, V_2, and V_0 are the magnitudes of positive-, negative-, and zero-sequence voltages, respectively. The corresponding fluxes produced by $\boldsymbol{v}_1$ and $\boldsymbol{v}_2$ are the positive-sequence flux ($\boldsymbol{\varphi}_{\mathrm{s1}}$) and negative-sequence flux ($\boldsymbol{\varphi}_{\mathrm{s2}}$), respectively, which is derived as (22). Both fluxes rotate at synchronous speed, whereas $\boldsymbol{\varphi}_{\mathrm{s1}}$ rotates in the opposite direction of $\boldsymbol{\varphi}_{\mathrm{s2}}$. Generally, there is the absence of a zero-sequence component as the generator is coupled through a star/delta transformer (Fig. 1) and hence, $\boldsymbol{v}_0$ does not produce any flux. The steady-state, the stator fluxes produced by positive- and negative-sequence stator voltages are expressed as follows:

$$\boldsymbol{\varphi}_{\mathrm{s1}} = \frac{V_1}{\mathrm{j}\omega_{\mathrm{s}}}\mathrm{e}^{\mathrm{j}\omega_{\mathrm{s}}t} \quad \text{and} \quad \boldsymbol{\varphi}_{\mathrm{s2}} = -\frac{V_2}{\mathrm{j}\omega_{\mathrm{s}}}\mathrm{e}^{-\mathrm{j}\omega_{\mathrm{s}}t} \tag{25}$$

In practice, the magnitude of the stator voltage falls suddenly at the occurrence of an asymmetrical/unbalanced fault scenario. Nevertheless, the stator flux does not follow the immediate change of stator voltage. An additional momentary flux (i.e. natural flux ($\boldsymbol{\varphi}_{\mathrm{sn}}$) component is seen in this scenario to maintain continuity of stator flux. Each stator flux produces a corresponding voltage in the rotor winding. Thus, the total stator flux is computed as (26) and the stator flux in the rotor reference frame is expressed as (27) [29]

$$\begin{aligned}&\boldsymbol{\varphi}_{\mathrm{s}} = \boldsymbol{\varphi}_{\mathrm{s1}} + \boldsymbol{\varphi}_{\mathrm{s2}} + \boldsymbol{\varphi}_{\mathrm{sn}}\\ &\Rightarrow \boldsymbol{\varphi}_{\mathrm{s}} = \frac{V_1}{\mathrm{j}\omega_{\mathrm{s}}}\mathrm{e}^{\mathrm{j}\omega_{\mathrm{s}}t} - \frac{V_2}{\mathrm{j}\omega_{\mathrm{s}}}\mathrm{e}^{-\mathrm{j}\omega_{\mathrm{s}}t} + \boldsymbol{\varphi}_{\mathrm{sn}}\mathrm{e}^{-(t/\tau_{\mathrm{s}})}\end{aligned} \tag{26}$$

$$\boldsymbol{\varphi}_{\mathrm{s}}^{\mathrm{r}} = \boldsymbol{\varphi}_{\mathrm{s}}\mathrm{e}^{-\mathrm{j}\omega_{\mathrm{r}}t} \tag{27}$$

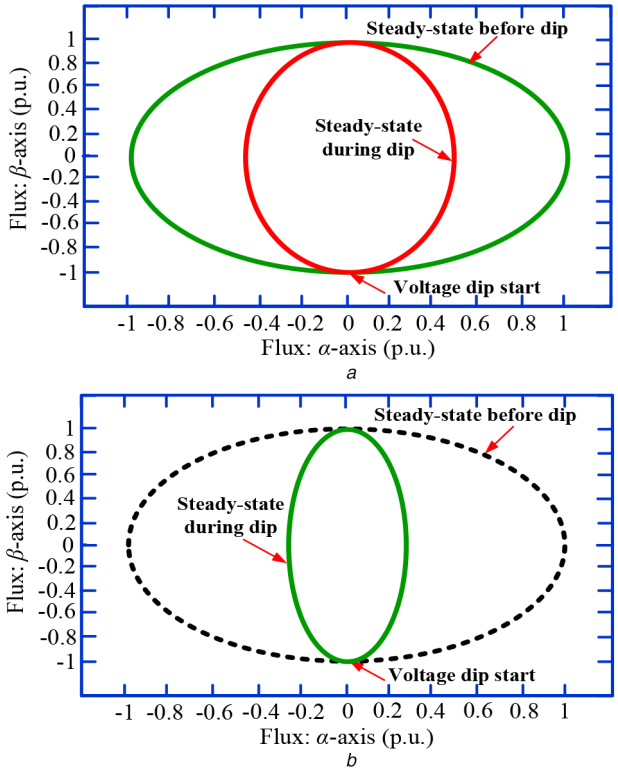

Fig. 4 *Trajectory for stator flux*
(a) 80% single-phase dip, ***(b)*** 60% single-phase starting at $t_0 = 0$

Now, the total open-circuit rotor voltage in the rotor reference frame is derived from (7), (25), and (26) which is expressed as follows:

$$\boldsymbol{v}_{\mathrm{r0}}^{\mathrm{r}} = \boldsymbol{v}_{\mathrm{r1}}^{\mathrm{r}} + \boldsymbol{v}_{\mathrm{r2}}^{\mathrm{r}} + \boldsymbol{v}_{\mathrm{rn}}^{\mathrm{r}} \Rightarrow \boldsymbol{v}_{\mathrm{r0}}^{\mathrm{r}} = V_1 \frac{L_{\mathrm{m}}}{L_{\mathrm{s}}} s \mathrm{e}^{\mathrm{j}s\omega_{\mathrm{s}}t} + V_2 \frac{L_{\mathrm{m}}}{L_{\mathrm{s}}} (s-2) \mathrm{e}^{\mathrm{j}(s-2)\omega_{\mathrm{s}}t} + \boldsymbol{v}_{\mathrm{rn}}^{\mathrm{r}} \tag{28}$$

From (28), it is obvious that the positive-sequence rotor voltage ($\boldsymbol{v}_{\mathrm{r1}}^{\mathrm{r}}$) is proportional to slip (s). However, the negative-sequence rotor voltage ($\boldsymbol{v}_{\mathrm{r2}}^{\mathrm{r}}$) includes a factor of 2. Hence, its amplitude may rise to a higher value when the asymmetrical ratio of the dip is high. As the value of slip (s) is small, the frequency of $\boldsymbol{v}_{\mathrm{r2}}^{\mathrm{r}}$ is approximately twice the grid frequency and the frequency of $\boldsymbol{v}_{\mathrm{r1}}^{\mathrm{r}}$ is equal to the slip frequency.

The rotor natural voltage ($\boldsymbol{v}_{\mathrm{rn}}^{\mathrm{r}}$) of the natural flux depends on its initial value and can be expressed as follows:

$$\boldsymbol{v}_{\mathrm{rn}}^{\mathrm{r}} = -\frac{L_{\mathrm{m}}}{L_{\mathrm{s}}} \left(\frac{1}{\tau_{\mathrm{s}}} + j\omega_{\mathrm{r}} \right) \varphi_{n0} \mathrm{e}^{-((t/\tau_{\mathrm{s}}) + \mathrm{j}\omega_{\mathrm{r}}t)} \tag{29}$$

Neglecting $1/\tau_{\mathrm{s}}$ in (29), $\boldsymbol{v}_{\mathrm{rn}}^{\mathrm{r}}$ is computed as follows:

$$\boldsymbol{v}_{\mathrm{rn}}^{\mathrm{r}} = -\mathrm{j}\omega_{\mathrm{r}} \frac{L_{\mathrm{m}}}{L_{\mathrm{s}}} \varphi_{n0} \mathrm{e}^{-((t/\tau_{\mathrm{s}}) + \mathrm{j}\omega_{\mathrm{r}}t)} \tag{30}$$

2.3.1 System operation under single-phase to ground (L–G) fault: Let us consider a L–G (i.e. phase-A to ground) fault with a dip (p) and the voltages of phase-B and phase-C are assumed to be unaffected. In this scenario, the phasors of three-phase voltages (i.e. $\boldsymbol{v}_a$, $\boldsymbol{v}_b$ and $\boldsymbol{v}_c$) in the phasor form can be expressed as follows [29]:

$$\boldsymbol{v}_a = V(1-p), \quad \boldsymbol{v}_b = \alpha^2 V \quad \text{and} \quad \boldsymbol{v}_c = \alpha V \tag{31}$$

where $\alpha = \mathrm{e}^{\mathrm{j}(2\pi/3)}$ is an operator and V is the magnitude of each phase voltage.

Furthermore, using the Fortescue transforms, the positive ($\boldsymbol{v}_1$), negative ($\boldsymbol{v}_2$) and zero-sequence ($\boldsymbol{v}_0$) voltage phasors are presented as follows:

$$\begin{bmatrix} \boldsymbol{v}_1 \\ \boldsymbol{v}_2 \\ \boldsymbol{v}_0 \end{bmatrix} = \frac{1}{3} \begin{bmatrix} 1 & \alpha & \alpha^2 \\ 1 & \alpha^2 & \alpha \\ 1 & 1 & 1 \end{bmatrix} \begin{bmatrix} V(1-p) \\ \alpha^2 V \\ \alpha V \end{bmatrix} = V \begin{bmatrix} (1-p/3) \\ -p/3 \\ -p/3 \end{bmatrix} \tag{32}$$

With the voltages expressed in (32), the positive- and negative-sequence fluxes using (25) and the corresponding voltages they induce in the rotor using (27) can be evaluated. Referring (15), the natural flux ($\boldsymbol{\varphi}_{\mathrm{sn}}$) can be obtained from the initial conditions by considering that the total flux must be continuous (i.e. flux must be identical immediately before and after the fault) as follows [29]:

$$\boldsymbol{\varphi}_{\mathrm{s}}(t_0^-) = \boldsymbol{\varphi}_{\mathrm{s}}(t_0^+) \Rightarrow \boldsymbol{\varphi}_{\mathrm{s}}(t_0^-) = \boldsymbol{\varphi}_{\mathrm{s1}}(t_0^+) + \boldsymbol{\varphi}_{\mathrm{s2}}(t_0^+) + \boldsymbol{\varphi}_{\mathrm{sn}}(t_0^+) \tag{33}$$

Unlike a symmetrical fault, the amplitude of the natural flux depends on the fault inception time in the case of the asymmetrical fault. Let us consider a L–G (i.e. phase-A to ground) fault with a dip (p) = 80% at $t_0 = 0$. In this case, $\boldsymbol{\varphi}_{\mathrm{sn}}(t_0 = 0)$ is zero since the positive and negative fluxes are aligned and their sum is equal to the flux before the fault as shown in Fig. 4*a*. From Fig. 4*a*, it can be observed that the trajectory traced by the flux is an elliptical shape. This is due to the fact that the positive flux rotates in the counter-clockwise direction, whereas the negative flux rotates in the clockwise direction. The major axis of the ellipse occurs when both the fluxes coincide in the same direction while the minor axis of the ellipse appears when they are aligned but in the opposite direction.

The trajectory traced by the flux for another phase-A to ground fault with a dip (p) = 60% at $t_0 = 0$ is shown in Fig. 4*b*. In Fig. 4*b*, it can be seen that the trajectory is elliptical, but it has shrunk radically. The same can be analysed for the asymmetrical fault on the other two phases (i.e. phase-B to ground and phase-C to ground). From these analyses, it can be concluded that the lower is the dip depth (p), the voltage induced by the stator flux does not exceed the voltage limit that the rotor converter can generate, the current remains under control. Under these circumstances (i.e. normal operation), the induced voltage in the rotor terminals does not substantially vary [22]. For larger dips, over-currents appear that increase as the depth of the dip becomes bigger. As the voltage induced by the stator flux exceeds the maximum safety limit of the converter, large transient currents are induced in the stator circuit. Consequently, the control of the current is lost transitorily.

2.3.2 System operation under a double-phase (i.e. phase-to-phase) fault: In this case study, a short-circuit between phases B and C is considered to analyse the effect of phase-to-phase (i.e. L–L) fault. The initiation of BC-fault results in voltage drops in phase-B and phase-C while the voltage of phase-A remains unaltered when the positive- and negative-sequence networks have equal impedance. For this fault, the three-phase voltages can be expressed as follows:

$$\boldsymbol{v}_a = V, \quad \boldsymbol{v}_b = V\left(\alpha^2 + \mathrm{j}\frac{\sqrt{3}}{2}p\right) \quad \text{and} \quad \boldsymbol{v}_c = \mathrm{V}\left(a - \mathrm{j}\frac{\sqrt{3}}{2}p\right) \tag{34}$$

After solving, from (34), it can be observed that the voltages of the phases B and C become closer with the increase of dip depth (p). However, the two voltages become equal at $p = 1$. Similar to Section 2.3.1, the positive-, negative-, and zero-sequence voltages can be calculated as follows [28]:

$$\begin{bmatrix} \boldsymbol{v}_1 \\ \boldsymbol{v}_2 \\ \boldsymbol{v}_0 \end{bmatrix} = V \begin{bmatrix} 1 - \frac{p}{2} \\ \frac{p}{2} \\ \frac{p}{2} \end{bmatrix} \tag{35}$$

Table 1 Positive-sequence (φ_1), negative-sequence (φ_2), and natural (φ_{sn}) stator fluxes during possible grid faults

Fault	φ_1	φ_2	φ_{sn}
single-phase to ground (L–G)	$1-p/3$	$p/3$	0 to $2p/3$
phase to phase (L–L)	$1-p/2$	$p/2$	0 to p
double-line to ground (L–L–G)	$1-2p/3$	$p/3$	$p/3$ to p
three-phase (L–L–L)	$1-p$	0	p

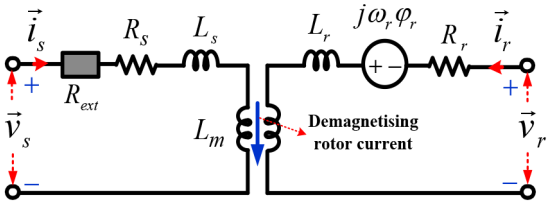

Fig. 5 *Equivalent diagram of DFIG with demagnetisation rotor current and external stator resistance for the stationary stator reference frame*

Correspondingly, using (34) and (35), the positive- and negative-sequence components of stator fluxes and rotor voltages can be computed.

The aforementioned study clearly shows that the operating behaviour of a grid-connected DFIG under the symmetrical grid fault is different as compared to the asymmetrical grid fault. Moreover, from (8) and (22), it can be seen that the rotor voltage ($\boldsymbol{v}_r^r$) is a function of rotor current ($\boldsymbol{i}_r^r$). During a symmetrical grid fault, an overvoltage is induced in the rotor windings due to the natural flux. Since this overvoltage is transitory in nature, the loss of current control occurs only during the period when the grid voltage changes abruptly (i.e. at the inception/clearance of the fault). Thus, a passive switchable circuit is used in the rotor circuit for limiting the rotor current and protecting the RSC from over-current as discussed in Section 2.2.

The loss of the rotor current depends on the overvoltage induced in the rotor winding. Since the rotor voltage is a function of the stator flux and each fault produces different flux performances, the induced rotor voltage and current nature will be different based on the nature of the fault. Relating to the fault dip depth (p), the per-unit values of the positive-sequence (φ_1), negative-sequence (φ_2) and natural (φ_{sn}) fluxes produced during different possible grid faults are summarised in Table 1. From Table 1, it can be depicted that for the same dip depth, the highest negative and natural fluxes are produced during phase-to-phase (i.e. L–L) fault. Hence, among various fault behaviours, the converter is more likely to lose current control (i.e. the converter will be affected severely due to higher over-current) will be during L–L fault. The system parameters should be within the threshold limits during the contingencies, otherwise, the protection schemes/circuits will be activated to protect the power system equipment and devices.

3 Proposed control strategies employed for DFIG-based WECS

The principle characteristics of the demagnetisation control strategy are as follows:

- The natural and negative-sequence components of the stator flux can be well balanced, thereby developed natural stator flux damping.
- The control strategy accelerates the minimising of stator and rotor currents, the transient response, the electromagnetic torque, the stator reactive power, and the DC-link voltage is reduced.
- To improve the system LVRT capability under a symmetrical and asymmetrical fault.

During the symmetrical grid fault, the phase voltages are balanced in nature. The negative-sequence components of the stator current and the stator flux are absent during a symmetrical fault. Meanwhile, the demagnetisation control is closely associated with the DC-stator flux. As a result, the symmetrical grid fault will affect the demagnetisation control.

In the proposed control strategy, a demagnetising current is injected in a direction opposite to that of the natural stator current ($\boldsymbol{i}_{sn}$) to minimise the effect of natural stator flux

$$\boldsymbol{i}_{rn}^{*} = -K\boldsymbol{i}_{sn} \tag{36}$$

where $\boldsymbol{i}_{rn}^{*}$ and $\boldsymbol{i}_{sn}$ are the reference natural rotor current and natural stator current, respectively. K is a constant value, which depends on the extent to which the desired current needs to be demagnetised.

Substituting (36) in (3), the natural stator flux ($\boldsymbol{\varphi}_{sn}$) can be calculated as follows:

$$\boldsymbol{\varphi}_{sn} = L_s\boldsymbol{i}_{sn} - L_mK\boldsymbol{i}_{sn} = (L_s - L_mK)\boldsymbol{i}_{sn} \tag{37}$$

Furthermore, inserting (37) into (1), the natural stator voltage ($\boldsymbol{v}_{sn}$) can be evaluated as follows:

$$\boldsymbol{v}_{sn} = R_s\boldsymbol{i}_{sn} + \frac{\mathrm{d}\boldsymbol{\varphi}_{sn}}{\mathrm{d}t} \tag{38}$$

Referring (13) and solving (38), the natural stator flux ($\boldsymbol{\varphi}_{sn}$) can be expressed as follows:

$$\boldsymbol{\varphi}_{sn} = \varphi_{n0}\mathrm{e}^{-(t/\tau_{s1})} = \varphi_{n0}\mathrm{e}^{-(R_s/L_s - KL_m)t}, \quad \tau_{s1} = \left(\frac{L_s - KL_m}{R_s}\right) \tag{39}$$

Comparing the time constants in (13) and (36), it can be concluded that the damping performance of $\boldsymbol{\varphi}_{sn}$ will be accelerated using the demagnetising current injection method. To achieve a larger damping performance of $\boldsymbol{\varphi}_{sn}$, an external resistance (R_{ext}) is inserted in the stator-side circuit of the DFIG. As a result, employing R_{ext}, a modified time constant (τ_{s2}) can be obtained in the demagnetisation control circuit and expressed as follows:

$$\tau_{s2} = \frac{L_s - KL_m}{R_s + R_{ext}} \tag{40}$$

The modified equivalent diagram of DFIG with demagnetisation rotor current and the external stator resistance for the stationary stator reference frame is shown in Fig. 5. From (39), it is clear that the damping performance of $\boldsymbol{\varphi}_{sn}$ will be accelerated with a higher value of K. However, the system turns out to be unstable due to the large value of K and the time constant sets off to a negative value. In this scenario, to ensure the stability guarantee of the system, it is necessary to estimate the critical value of K. Substituting $\tau_{s1} = 0$ in (39), the critical value of K (i.e. $K_{critical}$) is computed as follows:

$$K_{critical} = \frac{\text{Value of the stator inductance}}{\text{value of the mutual inductance}} = \frac{L_s}{L_m} \tag{41}$$

The rotor current of DFIG could be very high during severe grid-voltage dips (i.e. fault scenarios), resulting in an increased time of transitory oscillation and contributes a poor system dynamics. Hence, with the intention of reducing the time constant and improving the dynamic performances of the system during large dips, a series resistance-inductance ($R_p + L_p$) is connected in the rotor-side circuit as shown in Fig. 1. The main objective of L_p is to reduce high-frequency noises. The detailed function of the R_p and L_p is presented in Section 2.2. The time constant (τ_r) of the rotor circuit after inserting the series $R_p + L_p$ parameters is expressed as follows:

$$\tau_r = \left(\frac{\sigma L_r + L_p}{R_r + R_p}\right) \tag{42}$$

The block diagram of the proposed demagnetisation control strategy is shown in Fig. 6. The external stator resistance (R_{ext}) in series with a bandpass filter (BPF) is incorporated into the stator terminal for raising the natural stator current and hence, the stator flux during grid fault. There are three different types of frequencies (i.e. positive, negative, and natural) due to the presence of a three-phase sequence component in a DFIG-based WECS. To obtain a single frequency that will match the normal frequency, a BPF is used. In BPF, a certain range of frequency signals is allowed to pass through, which minimises the frequency of positive- and negative-sequence components. However, in the low-pass filter, the main drawback is that it passes the lowest value (i.e. takes the transitory flux value, which is 0 Hz). Hence, BPF makes the system less error efficient and more stable due to one frequency range. Meanwhile, R_{ext} accelerates the net resistance and thus, decreasing the time constant of the stator circuit as given in (40). This helps in damping the transitory stator flux at a faster rate. The increased natural stator current during grid fault helps in maintaining the rotor current, electromagnetic torque and DC-link voltage within their safe limit. Similar to a rotor switchable circuit (Fig. 1), R_{ext} is excluded (i.e. the power electronics switch will be closed and the path is short-circuited) from the stator-circuit to avoid unnecessary power loss and voltage drop during normal operation. The comparative signal between the actual stator current ($\boldsymbol{i}_s$) and the safe threshold stator current limit ($\boldsymbol{i}_{s-th}$) are employed to produce the switching pulses.

The reference active power (P^*_{ref}) and reactive power (Q^*_{ref}) can be expressed as (43) and (44), respectively [4]

$$P^*_{ref} = V_s \frac{L_m}{L_s} \boldsymbol{i}_{rq} \quad \text{and} \quad Q^*_{ref} = V_s \frac{L_m}{L_s} \boldsymbol{i}_{rd} - \frac{V_s^2}{\omega_s L_s} \tag{43}$$

$$\boldsymbol{i}^*_{rf} = \sqrt{\boldsymbol{i}^{*\,2}_{rd} + \boldsymbol{i}^{*\,2}_{rq}} \quad \text{and} \quad \boldsymbol{i}^*_r = \boldsymbol{i}^*_{rf} + \boldsymbol{i}^*_{rn} \tag{44}$$

where $\boldsymbol{i}^*_{rf}$ is the resultant reference synchronous rotor current, $\boldsymbol{i}^*_{rd}$ is the reference d-axis rotor current, $\boldsymbol{i}^*_{rq}$ is the reference q-axis rotor current, and $\boldsymbol{i}^*_{rn}$ is the reference natural rotor current.

Neglecting the stator resistance and assuming that the rotor currents are transformed into a synchronous reference frame where the q-axis is aligned with the grid voltage. The d-axis and q-axis current components can be provided together with the demagnetising current during grid fault. A limiter is used to restrict $\boldsymbol{i}^*_{rf}$ within −1.5 p.u. to +1.5 p.u. However, there is no need for a limiter for controlling i^*_{rn} as it is controlled by R_{ext}. To promote the DC-stator flux damping, the demagnetising current is prioritised over the active current. Finally, the synchronous current and the natural rotor current components are constrained to keep the rotor current in the safe limit as per the grid code requirements (GCRs).

In practice, the fundamental variables of the power system such as voltage, current, and frequency should be within the threshold limits (i.e. safety limits) during the system events/contingencies, otherwise, the protection schemes/circuits will be activated for a stable and secure operation [31, 32]. With the changing configuration of the power system and micro-grid/smart grid scenarios, each country updates its GCRs mainly emphasising the capability of LVRT on DFIG-WTs. To improve the power system reliability and stability, the DFIG-WTs ensure continuous operation during voltage dips (i.e. the rotor inrush current and DC-link overvoltage), as well as to minimise re-synchronisation problems after the clearance of faults for LVRT capability [30, 31]. Hence, it is ideal to make WTs stay connected to the power grid and provide support during transient periods as per the present GCRs. As per GCRs, the main LVRT grid criteria behaviours are characterised as follows [13, 14, 33]: (i) till 0.65 s after fault inception, the WTs shall remain connected to the grid. (ii) The permitted fault voltage (i.e. overvoltage) is 15% of its rated voltage. (iii) The voltage should be recovered to 90% of the rated voltage after the clearance of fault within 3 s. (iv) The DFIG needs to hold its connection state, at least for 150 ms when the terminal voltage drops to 20% of the nominal level. Meanwhile, the generator voltage should recovery to 75% of the nominal level within about 0.7 s. (v) The limit of the rotor current is set as 2 p.u. (vi) The electromagnetic torque is not exceeding 2–2.5 p.u. (vii) The stator current is limited to 2 p.u. Furthermore, as per the IEEE 1947-2003 standard, the WT shall connect to the grid during the LVRT to improve the stability of the power system. Additionally, the voltage fluctuation should be <±5% at the PCC during the system events and meet the flicker requirements as per the grid code [34, 35].

4 Results and discussion

To validate the effectiveness of the proposed modified demagnetisation control strategy, different comparative studies are presented using a standard DFIG-based wind system (Fig. 1). The simulation/modelling data of the DFIG-based power system are given in Table 2 [22, 24, 26]. In this study, the nominal value of the DC-link voltage (V^*_{dc}) is considered as 1150 V. Both symmetrical and asymmetrical grid fault scenarios are simulated on a 1.5MW DFIG-based WECS for analysis. In this study, the rated wind speed of the WT is 15 m/s. The supremacy performance of the proposed control scheme is compared with the two existing control strategies namely: (i) The conventional vector control (VC) scheme [24] and (ii) the IDC scheme [19], under both symmetrical and asymmetrical grid fault scenarios. The time-domain MATLAB/Simulink results are presented below to verify the effectiveness of the proposed controller.

4.1 Performance comparison under symmetrical three-phase (L–L–L) fault

In this case study, a symmetrical three-phase (L–L–L) fault is created at the time (t) = 0.6 s at the PCC in Fig. 1 and the fault continues for 150 ms. The dynamic responses of instantaneous stator voltage, rotor current, and stator current for the VC [24], IDC [19], and the proposed LVRT-control mechanisms are provided in Figs. 7–9, respectively.

From the graphs, it can be observed that the transient response/behaviour of the stator voltage, rotor current, and stator current are smoother (i.e. rise/dips) and less oscillatory in the proposed LVRT-control strategy as compared to the VC [24] and IDC [19]. Moreover, it is evident that the drop in stator voltage is less in the proposed LVRT-control strategy. During the fault, the deviations in stator current and rotor current lie within the safety limit followed by the grid code standards as compared to the aforementioned existing methodologies. Additionally, it can be realised that the IDC [19] provides better system performance for enhancing the low-voltage ride-through profile as compared to the existing VC [24]. In the existing VC [24], the rotor and stator current surpasses the safe limit as per the grid code and the stator voltage drop is very high and causes a very high transient phenomenon as shown in Fig. 7. In the IDC [19], the stator voltage drop and its transient response are less than the VC [24] as shown in Figs. 7 and 8. Correspondingly, the comparative dynamic responses of the root-mean-square (RMS) stator voltage ($V_{rms(stator)}$), electromechanical torque (T_{em}), and DC-link voltage (V_{dc}) for the above-mentioned control strategies are plotted in Fig. 10.

Fig. 10*a* exhibits that the voltage decline/drop in the $V_{rms(stator)}$ is relatively more in the conventional VC [24] and IDC [19] as compared to the proposed modified demagnetisation control, during the fault. In Fig. 10*b*, it can be depicted that using the proposed control strategy, the transient response of T_{em} is smothering and lie within the safety limit of 2.5 p.u. as compared to the other two existing LVRT methods. Moreover, Fig. 10*c* presents that the maximum overshoot in the V_{dc} lies below its safety limit for the proposed demagnetising method than the VC [24] and IDC [19]. From Fig. 10*c*, it can be observed that for the VC [24], the maximum overshoot in the V_{dc} goes above its safety limit of 2.5 p.u. and the maximum deviation in DC-link voltage lies exactly at the safety limit in the IDC [19]. For the above-mentioned control strategies, the performance statistical data/specifications of the minimum dip in $V_{rms(stator)}$ and T_{em}, and the maximum overshoot in V_{dc} are reported in Table 3.

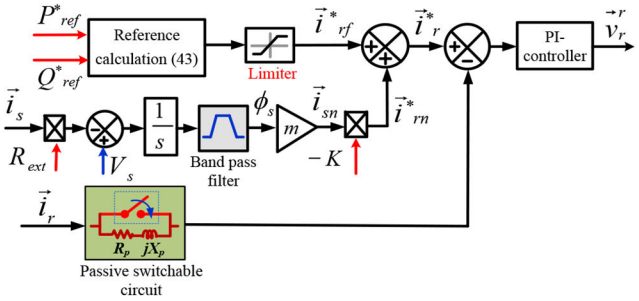

Fig. 6 *Block diagram of the proposed control strategy for the rotor reference frame*

Table 2 Simulated model parameters of DFIG based power system.

Modelling parameters/data	Symbol	Value
DFIG parameter		—
rated power	P_w	1.5 MW
rated stator voltage	V_s	585 V
rated frequency	f	50 Hz
stator leakage inductance	L_s	3.08 p.u.
rotor leakage inductance	L_r	3.06 p.u.
magnetising inductance	L_m	2.9 p.u.
stator to rotor turns ratio	n	3
stator resistance	R_s	0.023 p.u.
rotor resistance	R_r	0.016 p.u
generator inertia constant	H_g	0.685 s
turbine inertia constant	H_t	4.32 s
pairs of poles	P	3
rated rotor speed	ω_r	1 p.u.
damping coefficient	D_{sh}	0.01 p.u.
shaft stiffness coefficient	K_{sh}	0.5 p.u.
friction coefficient	B	0.01 p.u.
rotor transient inductance	σL_r	0.297 p.u.
external resistance	R_{ext}	1.71 Ω
demagnetising coefficient	K	0.97
passive resistance	R_p	1.13 Ω
passive inductance	L_p	0.034 H
Transformer parameters		—
rated kVA	P_{Tr}	12M VA
rated kV	V_1/V_2	0.585/25 kV
frequency	f	50 Hz
resistance	R_{T1}/R_{T2}	0.0017 p.u.
inductance	L_{T1}/L_{T2}	0.03 p.u.
magnetisation resistance	R_{TM}	500 p.u.
magnetisation reactance	L_{TM}	500 p.u.
converter and filter data		—
resistance of the grid-side filter	R_f	0.0032 p.u.
reactance of the grid-side filter	X_f	0.375 p.u.
switching frequency of the GSC	f_{ss}	5 kHz
switching frequency of the RSC	f_{sr}	2 kHz
DC-link capacitor	C_{dc}	5000×10^{-6} F
DC-link voltage	V_{dc}	1150 V
transmission line length	l	30 km
line positive-sequence resistance	R_{tp}	0.1153 Ω/km
line zero-sequence resistance	R_{t0}	0.413 Ω/km
line positive-sequence inductance	L_{tp}	1.05 mH/km
line zero-sequence inductance	L_{t0}	3.32 mH/km
line positive-sequence inductance	C_{tp}	1.33 nF/km
line zero-sequence inductance	C_{t0}	5.01 nF/km

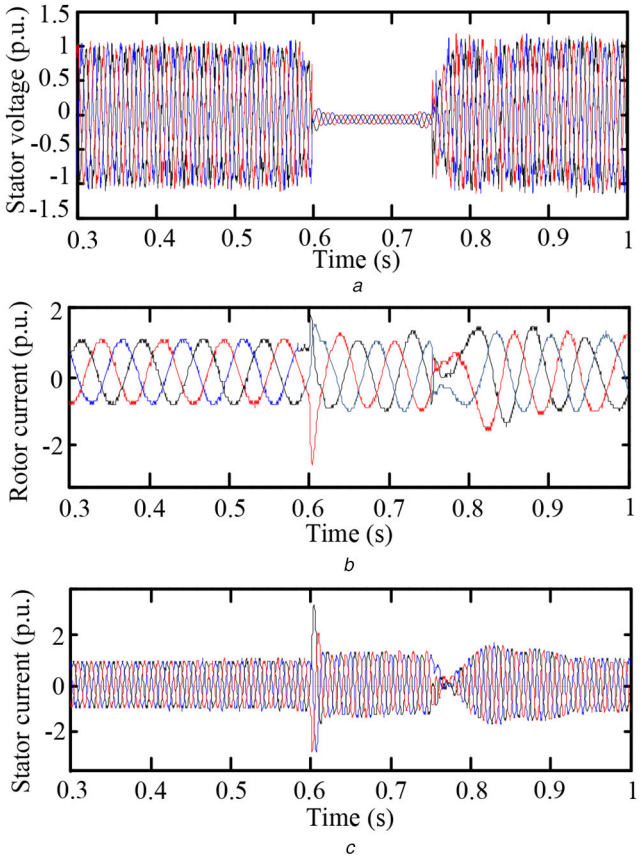

Fig. 7 *Simulation result under symmetrical L–L–L fault using VC*
(a) Stator voltage, ***(b)*** Rotor current, ***(c)*** Stator current

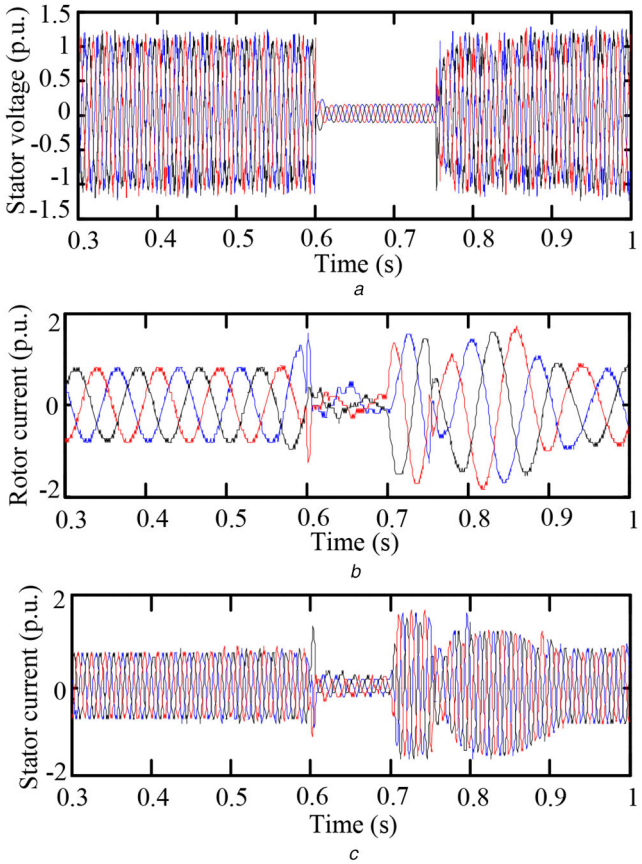

Fig. 8 *Simulation result under symmetrical L–L–L fault using improved demagnetisation-based control*
(a) Stator voltage, ***(b)*** Rotor current, ***(c)*** Stator current

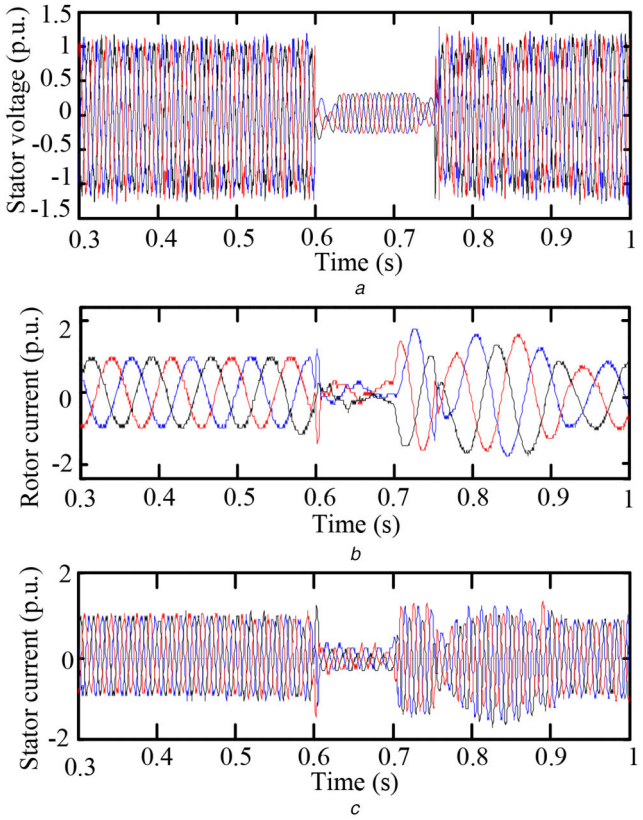

Fig. 9 *Simulation result under symmetrical L–L–L fault using the proposed control*
(a) Stator voltage, ***(b)*** Rotor current, ***(c)*** Stator current

4.2 Performance comparison under asymmetrical (L–G) fault

In this case study, an asymmetrical (L–G) fault scenario is considered to verify the efficacy of the control strategy on the proposed LVRT control of the DFIG-based wind system. A L–G fault occurs at $t = 0.5$ s on phase-A, and the duration of the fault is 150 ms as illustrated in Figs. 11–14. Figs. 11–13 illustrate the instantaneous waveforms of the stator voltage, rotor current, and stator current for each of the control methods (i.e. the existing VC [24] and IDC [19] and the proposed method). Fig. 14 presents the comparative dynamic responses of the RMS stator voltage ($V_{\text{rms(stator)}}$), electromechanical torque (T_{em}), and DC-link voltage (V_{dc}) for the aforesaid control strategies.

From Figs. 11–14, it can be depicted that the proposed control strategy exhibits a superior dynamic performance (i.e. lower oscillations and transient phenomenon) relatively than the VC [24] and IDC [19]. Moreover, it can be observed that in the proposed control, the system parameters such as stator current, rotor current, $V_{\text{rms(stator)}}$, T_{em}, and V_{dc} are within the permissible limit regarding the LVRT requirements of the DFIG-based wind system as per the grid code criterion. The exact values of minimum undershoot in $V_{\text{rms(stator)}}$ and T_{em}, and the maximum overshoot in V_{dc} of DFIG-based system subjected to the asymmetrical (L–G) fault is given in Table 4. The same can be analysed for the asymmetrical fault on the other phases (i.e. phases B and C). From the above discussion, it is evident that the asymmetrical fault gives rise to more obvious oscillations in the stator current, rotor current, electromagnetic torque, and the DC-link voltage as compared to the symmetrical fault.

4.3 Performance evaluation of the proposed control method under asymmetrical (double-phase to ground) fault

Furthermore, an asymmetrical double-line to ground (L–L–G) fault is accomplished to validate the usefulness of the proposed LVRT-control topology. In this case, phases A and B to ground fault at $t =$ 0.5–0.65 s is considered. The dynamic performance of the stator voltage, rotor current, stator current, T_{em} and V_{dc} for the L–L–G

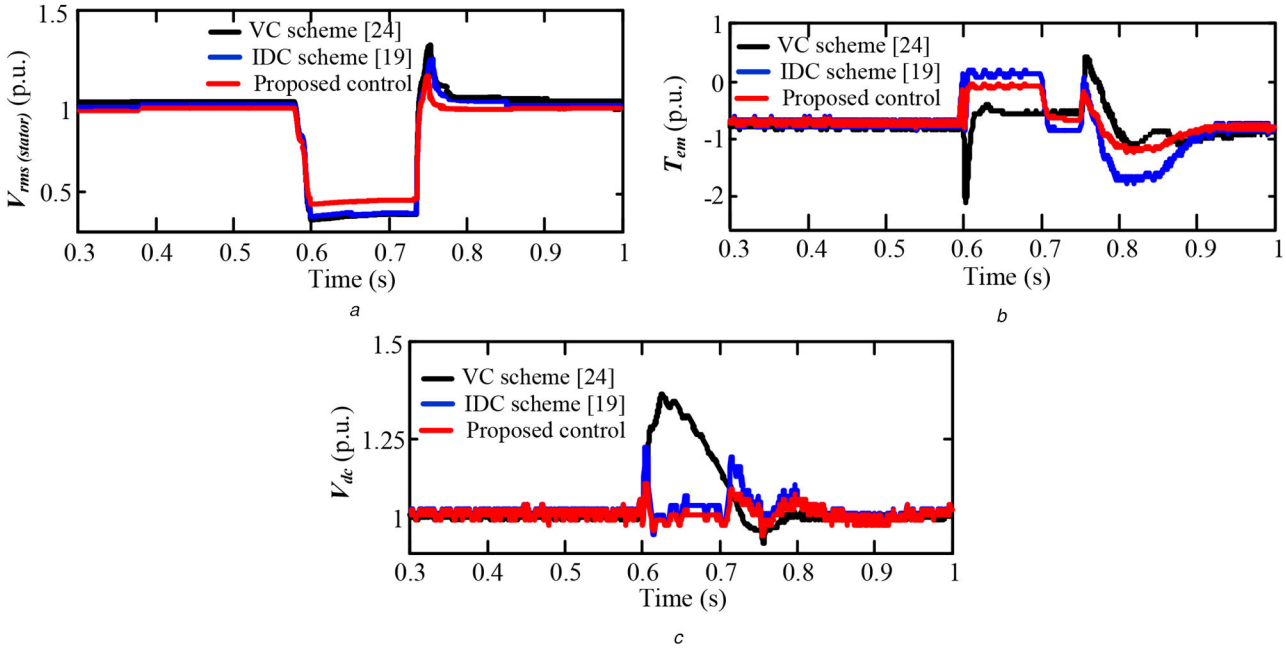

Fig. 10 *Simulation result under symmetrical L–L–L fault*
(a) RMS stator voltage (V), ***(b)*** Electromagnetic torque (T_{em}), ***(c)*** DC-link voltage (V_{dc})

Table 3 Comparative performance indexes in $V_{rms(stator)}$, T_{em}, and V_{dc} during the symmetrical L–L–L fault

Parameters	VC [24]	IDC [19]	Proposed scheme
minimum dip in $V_{rms\ (stator)}$	0.055 p.u	0.12 p.u.	0.25 p.u.
minimum dip in T_{em}	2.72 p.u.	1.8 p.u.	1.31 p.u.
maximum overshoot in V_{dc}	1.35 p.u.	1.2 p.u.	1.05 p.u.

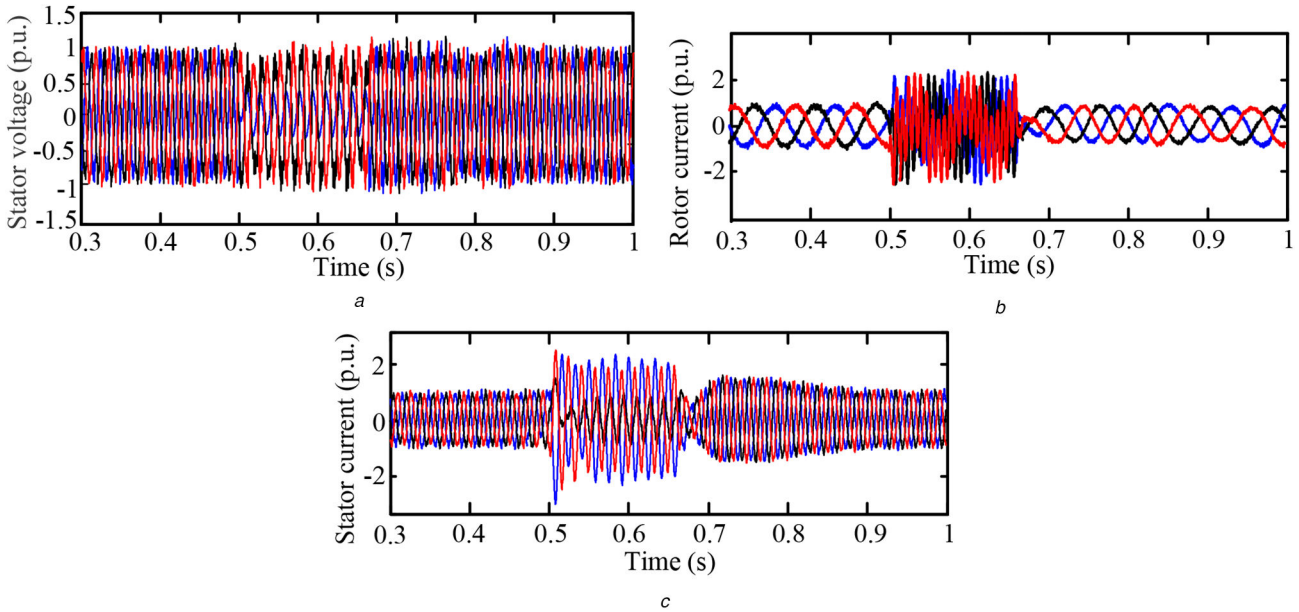

Fig. 11 *Simulation result under asymmetrical L–G fault using VC*
(a) Stator voltage, ***(b)*** Rotor current, ***(c)*** Stator current

fault are shown in Fig. 15. From Fig. 15*a*, it can be observed that the distortions in the stator voltages of two faulty phases are relatively more (i.e. decreased from 1 to 0.48 p.u.), whereas the voltage of the healthy phase is decreased from 1 to 0.9 p.u., during the fault period. As shown in Figs. 15*b* and *c*, the proposed control strategy is able to restore the rotor and stator current to their nominal value after the clearance of the fault without any sharp distortion. From Fig. 15*d*, it is seen that the electromagnetic torque is suddenly decreased from −0.5 to −1.5 p.u. at the initiation of the time of fault, which is below the safety limit. Moreover, the DC-link voltage slightly increases from 1 to 1.135 p.u. at the initiation of the fault as shown in Fig. 15*e*. The same observations have been noticed for the other double phases to ground fault.

For the above L–L–G fault, the harmonic analysis is examined during the stator voltage dip at $t = 0.5$s from Fig. 15*a*. The comparative total harmonic distortion (THD) graph during the voltage dip for without and with the proposed control scheme is plotted in Fig. 16. From the graph, the obtained exact value of the THD injected to the grid due to the stator voltage without and with the proposed control scheme are 5.41 and 3.25%, respectively. From the results, it is found that the THD of the stator voltage injected into the grid is satisfactory as per the requirement of the

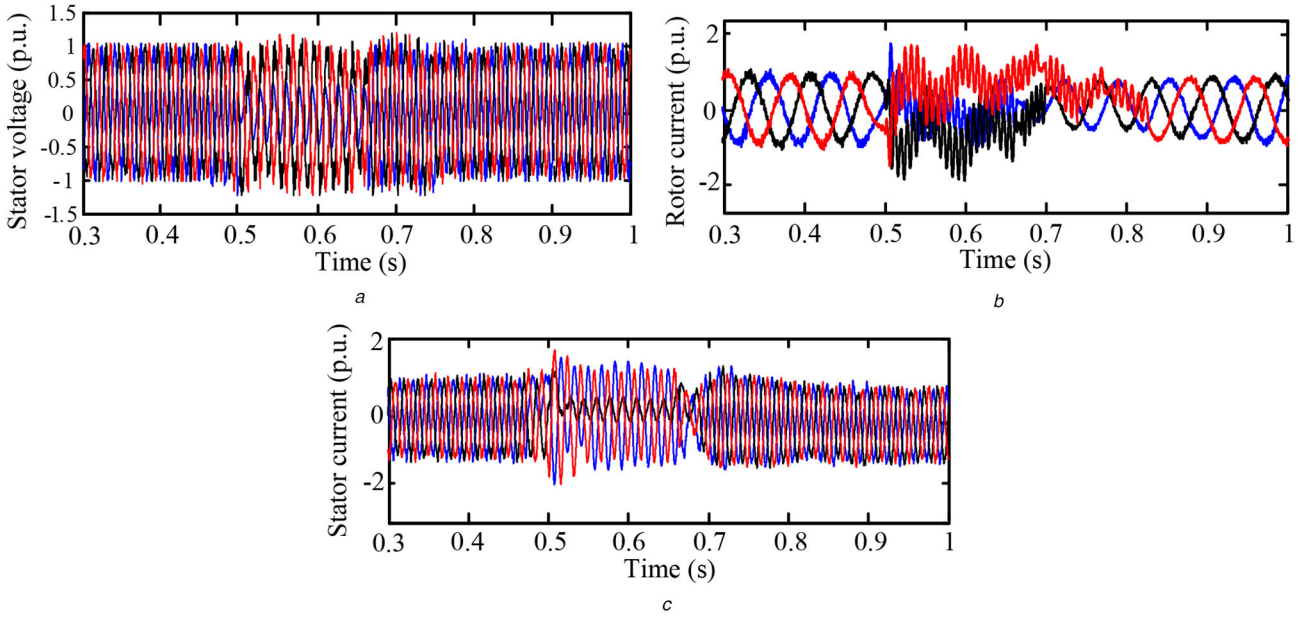

Fig. 12 *Simulation result under asymmetrical L–G fault using IDC*
(a) Stator voltage, ***(b)*** Rotor current, ***(c)*** Stator current

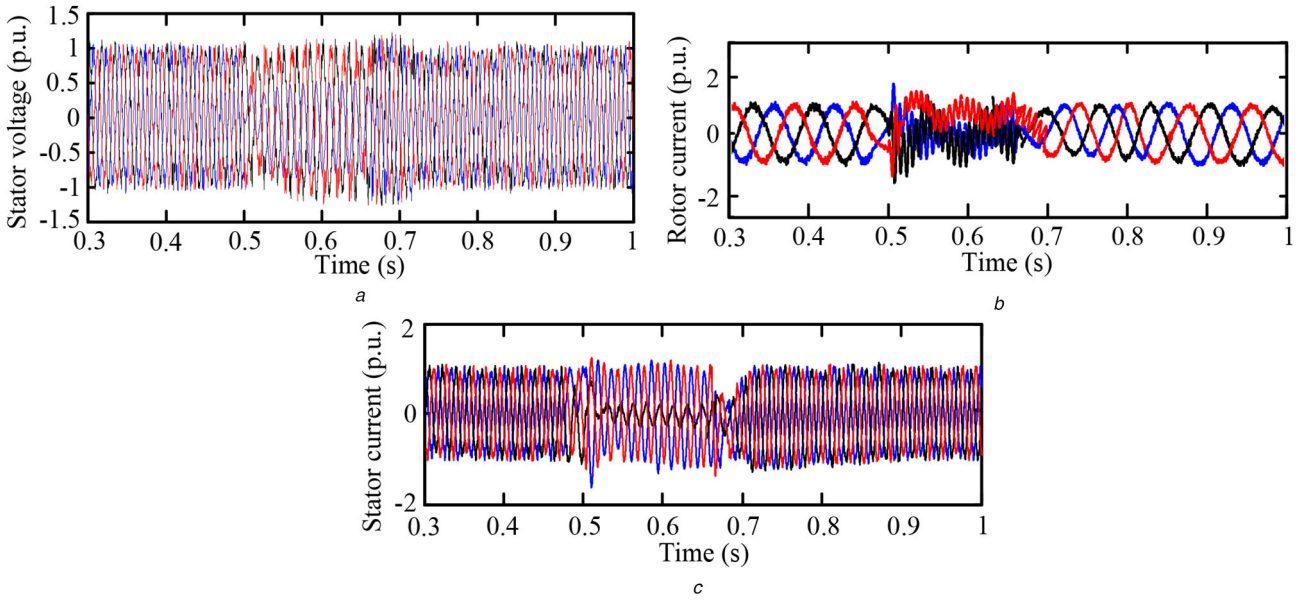

Fig. 13 *Simulation result under asymmetrical L–G fault using the proposed control*
(a) Stator voltage, ***(b)*** Rotor current, ***(c)*** Stator current

IEEE 1947–2003 standard limits (i.e. THD level <5%) in the proposed controller [34, 35]. In practice, the generation of harmonics is primarily caused due to the switching of the RSC, GSC, and DC offset of transient current appeared during the voltage dip. From the above studies, it can be established that the proposed control scheme improves the LVRT capability under transient conditions as per the grid code standard as highlighted in [13, 33].

5 Conclusion

This paper presents a modified demagnetisation control strategy and an external resistance in the stator side and rotor side of the DFIG to enhance the LVRT capability of DFIG-based WECS. The addition of external resistance in the stator accelerates the damping of the transient flux by decreasing the time constant. With the demagnetising control strategy, the transient responses of rotor current, stator current, electromagnetic torque, and DC-link voltage of the DFIG-based WECS are notably enhanced at the initiation and clearance under both symmetrical and asymmetrical grid faults. Hence, the possibility of damage to the converters can be avoided by using the proposed control approach and system LVRT capability is improved. The comparative results clearly show that the proposed control strategy exhibits a better performance concerning the LVRT profile as compared to the existing control strategies. Due to better dynamic responses and the above-mentioned system parameters lie within the safety limit concerning the LVRT performance, the proposed control strategy improves the stability and security operations of the power system. Hence, the proposed control approach can comply with the GCRs with the capability of LVRT on DFIG-WTs with the changing scenario of the higher penetration of wind generation.

6 Acknowledgments

The authors are very grateful to the Arctic Centre for Sustainable Energy (ARC), UiT The Arctic University of Norway, Norway for providing an environment to do this research.

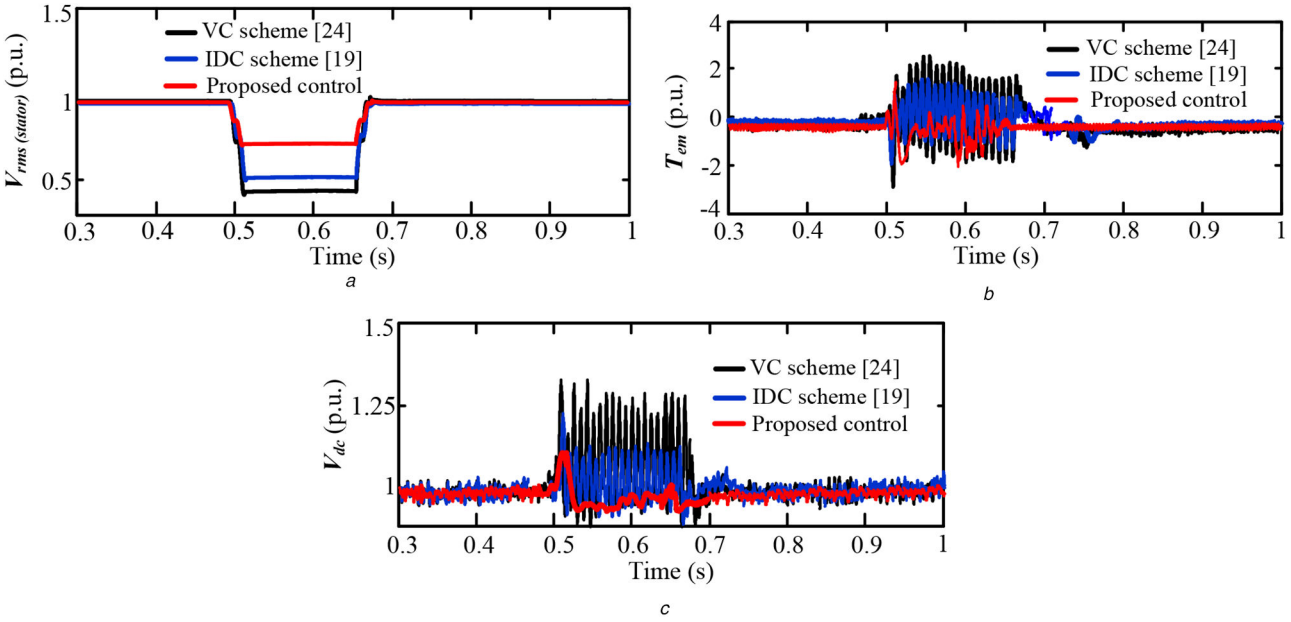

Fig. 14 *Simulation result under asymmetrical L–G fault*
(a) RMS stator voltage, ***(b)*** Electromagnetic torque (T_{em}), ***(c)*** DC-link voltage (V_{dc})

Table 4 Comparative performance indexes in $V_{rms(stator)}$, T_{em}, and V_{dc} during the asymmetrical L–G fault

Parameters	VC [24]	IDC [19]	Proposed scheme
minimum dip in $V_{rms\ (stator)}$	0.51 p.u.	0.42 p.u.	0.25 p.u.
minimum dip in T_{em}	3.05 p.u.	2.25 p.u.	2.0 p.u.
maximum overshoot in V_{dc}	1.3 p.u.	1.21 p.u	1.11 p.u.

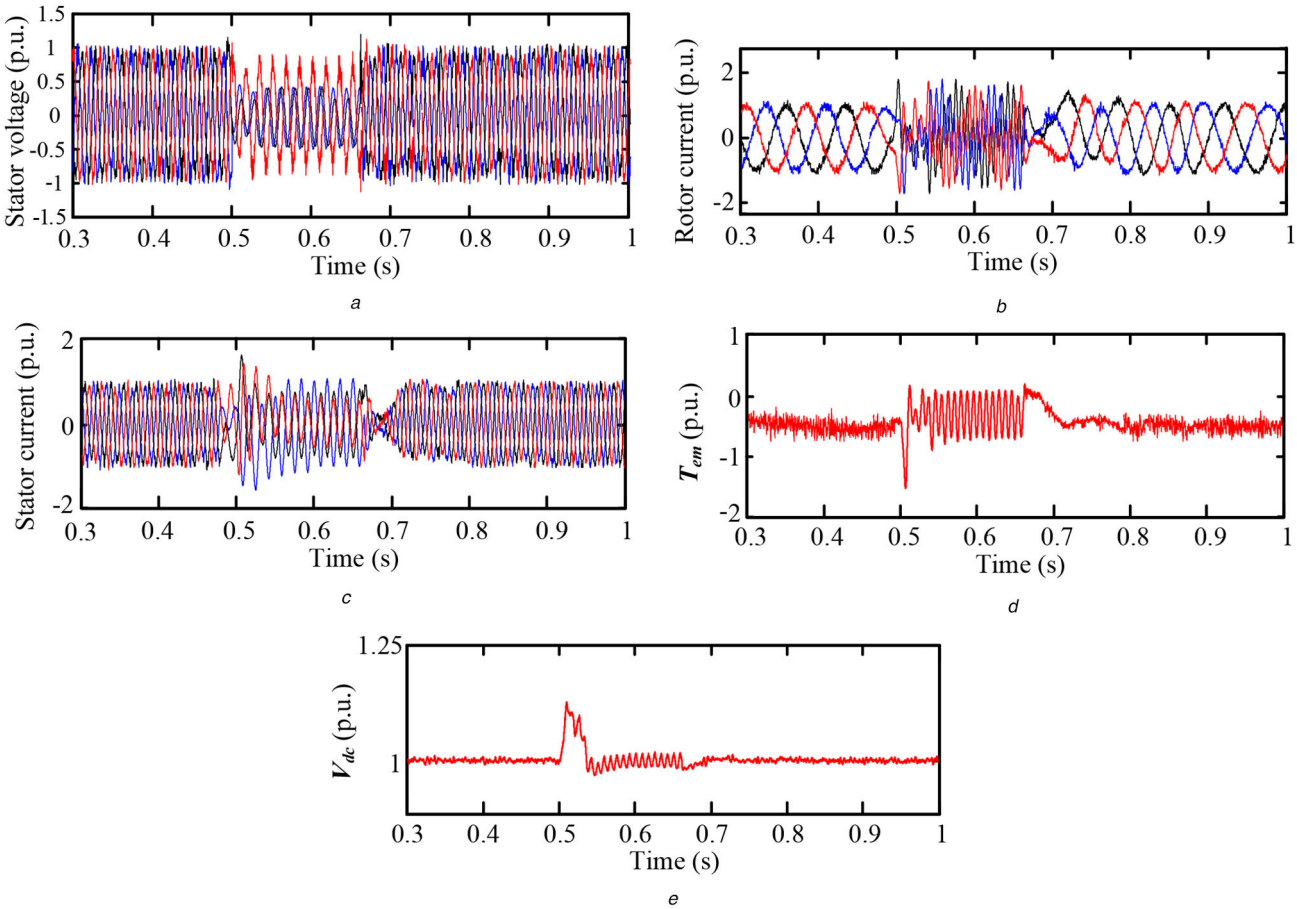

Fig. 15 *Simulation result under asymmetrical L–L–G fault using the proposed LVRT control*
(a) Stator voltage, ***(b)*** Rotor current, ***(c)*** Stator current, ***(d)*** Electromagnetic torque, ***(e)*** DC-link voltage

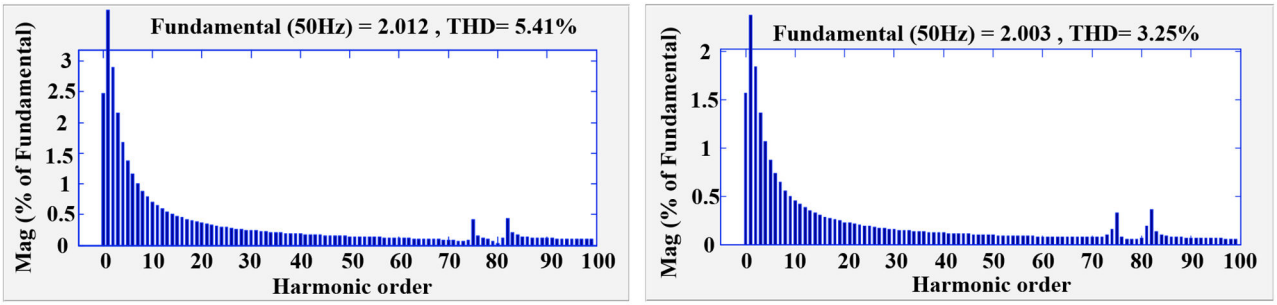

a *b*

Fig. 16 *THD of grid injected stator voltage*
(a) Without any control strategy, ***(b)*** With the proposed LVRT-control strategy

7 References

[1] Hossain, M.M., Ali, M.H.: 'Future research directions for the wind turbine generator system', *Renew. Sustain. Energy Rev.*, 2015, **49**, pp. 481–489

[2] Tourou, P., Sourkounis, C.: 'Review of control strategies for DFIG based wind turbines under unsymmetrical grid faults'. 9th Int. Conf. on Ecological Vehicle and Renewable Energies, Monte-Carlo, Monaco, 25–27 March 2014, pp. 1–9

[3] Li, H., Chen, Z.: 'Overview of different wind generator systems and their comparisons', *IET Renew. Power Gener.*, 2008, **2**, (2), pp. 123–138

[4] Muller, S., Deicke, M., De Doncker, R.W.: 'Doubly fed induction generator systems for wind turbines', *IEEE Ind. Appl. Mag.*, 2002, **8**, (3), pp. 26–33

[5] Hughes, F.M., Anaya-Lara, O., Jenkins, N., *et al.*: 'Control of DFIG-based wind generation for power network support', *IEEE Trans. Power Syst.*, 2005, **20**, (4), pp. 1958–1966

[6] Marques, G.D., Sousa, D.M.: 'Understanding the doubly fed induction generator during voltage dips', *IEEE Trans. Energy Convers.*, 2012, **27**, (2), pp. 421–461

[7] The grid code. Available at http//www.nationalgrid.com/uk/Electricity/Codes/gridcode

[8] Pannell, G., Atkinson, D.J., Zahawi, B.: 'Minimum-threshold crowbar for a fault-ride-through grid-code-compliant DFIG wind turbine', *IEEE Trans. Energy Convers.*, 2010, **25**, (3), pp. 750–759

[9] Meegahapola, L.G., Littler, T., Flynn, D.: 'Decoupled-DFIG fault ride through strategy for enhanced stability performance during grid faults', *IEEE Trans. Sustain. Energy*, 2010, **1**, (3), pp. 152–162

[10] Qiao, W., Venayagamorthy, G.K., Harley, R.G.: 'Real-time implementation of a STATCOM on a wind farm equipped with doubly fed induction generators', *IEEE Trans. Ind. Appl.*, 2009, **45**, (1), pp. 98–107

[11] Liang, J., Qiao, W., Harley, R.G.: 'Feed-forward transient current control for low-voltage ride-through enhancement of DFIG wind turbines', *IEEE Trans. Energy Convers.*, 2010, **25**, (3), pp. 836–843

[12] Liang, J., Howard, F.H., Restrepo, J.A., *et al.*: 'Feed-forward transient compensation control for DFIG wind turbines during both balanced and unbalanced grid disturbances', *IEEE Trans. Ind. Appl.*, 2013, **49**, (3), pp. 1452–1463

[13] Mahela, O.P., Gupta, N., Khosravy, M., *et al.*: 'Comprehensive overview of low voltage ride through methods of grid integrated wind generator', *IEEE Access*, 2019, **7**, pp. 99299–99326

[14] Qin, B., Li, H., Zhou, X., *et al.*: 'Low-voltage ride-through techniques in DFIG-based wind turbines: a review', *Appl. Sci.*, 2020, **10**, (6), pp. 1–25

[15] Hossain, M.J., Saha, T.K., Mithulananthan, N., *et al.*: 'Control strategies for augmenting LVRT capability of DFIGs in interconnected power systems', *IEEE Trans. Ind. Electron.*, 2013, **60**, (6), pp. 2510–2522

[16] Zhu, R., Chen, Z., Wu, X., *et al.*: 'Virtual damping flux-based LVRT control for DFIG-based wind turbine', *IEEE Trans. Energy Convers.*, 2015, **30**, (2), pp. 714–725

[17] Hu, S., Lin, X., Kang, Y., *et al.*: 'An improved low-voltage ride-through control strategy of doubly fed induction generator during grid faults', *IEEE Trans. Power Electron.*, 2011, **26**, (12), pp. 3653–3665

[18] Zhou, L., Liu, J., Zhou, S., *et al.*: 'Research of LVRT capability of DFIG with demagnetization control'. IEEE Energy Conversion Congress and Exposition, Denver, CO, USA, 15–19 September 2013

[19] Zhou, L., Liu, J., Zhou, S.: 'Improved demagnetization control of a doubly fed induction generator under balanced grid fault', *IEEE Trans. Power Electron.*, 2015, **30**, (12), pp. 6695–6705

[20] Huang, Q., Zou, X., Zhu, D., *et al.*: 'Scaled current tracking control for doubly fed induction generator to ride through serious grid faults', *IEEE Trans. Power Electron.*, 2016, **30**, (99), pp. 2150–2165

[21] Wen, G., Chen, Y., Zhong, Z., *et al.*: 'Dynamic voltage and current assignment strategies of nine-switch-converter-based DFIG wind power system for low-voltage ride-through (LVRT) under symmetrical grid voltage dip', *IEEE Trans. Ind. Appl.*, 2016, **52**, (4), pp. 3422–3434

[22] Mohammsdi, J., Afsharnia, S., Vaez-Zadeh, S.: 'Efficient fault-ride-through control strategy of DFIG-based wind turbines during the grid faults', *Energy Convers. Manage.*, 2014, **78**, pp. 88–95

[23] Mohammadi, J., Afsharnia, S., Vaez-Zadeh, S., *et al.*: 'Improved fault ride through strategy for doubly fed induction generator based wind turbines under both symmetrical and asymmetrical grid faults', *IET Renew. Power Gener.*, 2016, **10**, (8), pp. 1114–1122

[24] Mohammadi, J., Afsharnia, S., Ebrahimzadeh, E., *et al.*: 'An enhanced LVRT scheme for DFIG based WECSs under both balanced and unbalanced grid voltage sags', *Electr. Power Compon. Syst.*, 2017, **45**, (11), pp. 1242–1252

[25] Wang, M., Shi, Y., Zhang, Z., *et al.*: 'Synchronous flux weakening control with flux linkage prediction for doubly-fed wind power generation systems', *IEEE Access*, 2017, **5**, pp. 5463–5470

[26] Naderi, S.B., Negnevitsky, M., Muttaqi, K.M.: 'A modified dc chopper for limiting the fault current and controlling the dc-link voltage to enhance fault ride-through capability of doubly-fed induction-generator-based wind turbine', *IEEE Trans. Ind. Appl.*, 2019, **55**, (2), pp. 2021–2032

[27] Abad, G., López, J., Rodriguez, M.A., *et al.*: '*Doubly fed induction machine: modeling and control for wind energy generation*' (Wiley, Hoboken, NJ, USA, 2011)

[28] López, J., Sanchis, P., Roboam, X., *et al.*: 'Dynamic behaviour of the doubly-fed induction generator during three-phase voltage dips', *IEEE Trans. Energy Convers.*, 2007, **22**, (3), pp. 709–717

[29] López, J., Gubía, E., Sanchis, P., *et al.*: 'Wind turbines based on doubly fed induction generator under asymmetrical voltage dips', *IEEE Trans. Energy Convers.*, 2008, **23**, (1), pp. 321–330

[30] Fortescue, C.L.: 'Method of symmetrical co-ordinates applied to the solution of polyphase networks', *Trans. Am. Inst. Electr. Eng.*, 1918, **XXXVII**, (2), pp. 1027–1140

[31] Pradhan, C., Bhende, C.N., Samanta, A.K.: 'Adaptive virtual inertia based frequency regulation in wind integrated power system', *Renew. Energy*, 2018, **115**, pp. 558–574

[32] Zhang, D., Xu, H., Qiao, L., *et al.*: 'LVRT capability enhancement of DFIG based wind turbine with coordination control of dynamic voltage restorer and inductive fault current limiter', *PLoS ONE*, 2019, **14**, (8), pp. 1–24

[33] Jerin, A.R.A., Kaliannan, P., Subramaniam, U., *et al.*: 'Review on FRT solutions for improving transient stability in DFIG-WTs', *IET Renew. Power Gener.*, 2018, **12**, (15), pp. 1786–1799

[34] Mansouri, M.M., Nayeripour, M., Negnevitsky, M.: 'Internal electrical protection of wind turbine with doubly fed induction generator', *Renew. Sustain. Energy Rev.*, 2016, **55**, pp. 840–855

[35] IEEE 1547-2003: 'Standard for interconnecting distributed resources with electric power systems'